Nested Gaussian Laser Beams - A Blue-Detuned One-Dimensional Lattice of Optical Dipole Traps for Quantum Computing

A Senior Project
presented to
the Faculty of the Physics Department
California Polytechnic State University, San Luis Obispo

In Partial Fulfillment of
the Requirements for the Degree
Bachelor of Science

By

Travis Daniel Frazer

March, 2013

Table of Contents

List of Figures and Tables:

Figures:

Tables:

Introduction

Since its conception, quantum computation has generated a lot of interest. People from widely varied disciplines of physics are working to build quantum computers out of everything from neutral atoms to superconductors [1-6]. There is such a large effort towards building a quantum computer because theorized quantum algorithms are predicted to be able to perform a handful of tasks which are impossible for a standard, classical computer in any reasonable time scale [7]. Among these are Shor's algorithm for prime factorization [8], and Grover's search algorithm [9].

A quantum computer is unlike modern computers in that its constituent components predominantly obey quantum mechanics rather than classical mechanics. So, whereas a classical computer is made out of bits which can have a value of 1 or 0, the quantum bits (qubits) which make up a quantum computer can be in a state of both 0 and 1 at the same time due to quantum superposition. Furthermore, two qubits can be entangled, so their values are interdependent. This has been demonstrated with neutral atoms [10, 11] among other methods. By utilizing such quantum mechanical properties, quantum algorithms perform computations in a way impossible for classical computers. In a handful of important cases, this also leads to a decrease in computation time from beyond human time scales to more reasonable values [7].

Out of the many approaches to physically implementing a quantum computer, we are working in the field of neutral atom quantum computing. In this approach, neutral atoms are the quantum mechanical objects used as qubits. For a stable quantum computer, the atoms must be predictably confined, and it is easiest if they are also individually addressable [12]. The atoms are addressed with a separate probe laser, so only the geometry of the traps limits how addressable the individual atoms are. To confine the atoms, dipole trapping is usually used.

In dipole trapping, the interaction between a neutral, polarizable particle and the oscillating electric field of an electromagnetic wave confines the particle to one location. Depending on whether the wave's frequency is “blue-detuned” or “red-detuned,” the particle will be drawn to either intensity minima, or maxima respectively [13]. A blue detuned wave has a slightly higher frequency than the natural frequency of the particle, while a red-detuned wave's frequency is slightly lower.

Thus, to individually confine a large set of atoms to make many qubits, a large set of localized intensity minima (dark spots) or maxima (bright spots) is needed. One extensively used way of generating such a lattice in one dimension (1D) is with two counter-propagating Gaussian laser beams. The two traveling waves create a standing wave, and the anti-nodes along the beams' axis form bright spots capable of red-detuned trapping [14]. Note that this setup does not work, however, for blue-detuned trapping; there would be no radial confinement for atoms placed in the nodes.

Red-detuned trapping has disadvantages in terms of qubit stability compared to blue-detuned trapping [15]. The atoms are more likely to spontaneously leave the desired state because they are held in bright spots where there are the most photons to interact with. As mentioned above, though red-detuned 1D lattices are common, blue-detuned 1D lattices are challenging to produce. It was our goal to solve this problem, and create a blue-detuned 1D lattice of dipole traps.

The arrangement of Gaussian beams we conceived of to produce the blue-detuned 1D lattice is actually very similar to the red-detuned case. The only difference is that one beam has a smaller profile so that

the two beams do not perfectly overlap and interfere in the radial direction. Qualitatively, the standing wave pattern is still produced within the smaller beam's radius, but no standing wave pattern is produced beyond it, leaving essentially just the outer beam's light. Thus the nodes are surrounded on all sides by higher intensity light, creating the dark spot geometry necessary for blue-detuned dipole trapping. After a thorough literature search, we were pleased to discover that this pattern had been explored for atom trapping and successfully published by Zemánek and Foot in 1998 [16].

This beam arrangement could have applications ranging from quantum computation, to quantum simulation, to an atomic conveyor belt. For this paper, however, we investigated only the basic dipole trap properties of interest to quantum computing. Other quantum information applications would have similar requirements of the traps. We computationally investigated the beam arrangement, and will present our findings on its basic geometric properties, and its basic dipole trapping properties.

1 Theory of Trapping Atoms with Light for Quantum Computing

1.1 Neutral Atom Quantum Computing

Neutral atom quantum computing is one of many methods being pursued in an attempt to physically implement a quantum computer. In this method, neutral atoms, usually alkalis like rubidium or cesium, are used as the qubits. Because the qubits must be very stable and finely controlled, this necessitates the trapping of individual atoms not only in one location, but in one chosen state for suitably long periods of time.

The five requirements for implementing a quantum computer, as stated by DiVincenzo, are a scalable physical system with well characterized qubits, the ability to initialize the state of the qubits to a simple fiducial state (i.e. |000...>), decoherence times much larger than the gate operation time, a universal set of quantum gates, and a qubit specific measurement capability [12]. We will consider each of these in turn in the context of neutral atoms in dipole traps as qubits.

A scalable system is the main requirement still eluding neutral atom quantum computing. Three dimensional optical lattices may be used, but the inaccessibility of internal traps limits the useful scalability of this design [1]. Thus, 2D arrays of traps are being investigated as a solution to the problem of scalability. The 1D lattice of traps investigated in this paper could also be scaled up to hold a large number of qubits, but it remains to be seen whether this would be more effective for a full scale quantum computer, or another quantum information application.

Two internal states of the neutral atom are taken to be the qubit states (|0> and |1>). That is, among the possible states of the valence electron, two are carefully chosen to be the qubit states. Usually, the chosen states are within the hyperfine ground state manifold to increase the decoherence time [1]. Alkali atoms have a particularly suitable structure of states for this application. Transferring the qubits between states is done either with microwave radiation, or with two lasers with an energy difference that matches the transition energy between the states.

A long decoherence time is one of the inherent benefits of using neutral atoms for quantum computing. The ground states involved have naturally long lifetimes. So long as the atoms are well cooled and isolated from their environment, many operations (i.e. laser pulses) can be accomplished before the atoms will transition to an excited state. A long decoherence time is also a benefit of the 1D lattice we

are investigating. As we shall see, blue-detuned traps hold the atoms in intensity minima, lowering scattering effects and lengthening the decoherence time in comparison to red-detuned traps, where the atoms are held in intensity maxima.

A set of gates consisting of a two-qubit "cPHASE" gate and single qubit gates is sufficient to implement any quantum circuit. Recently, cPHASE gates have been realized with neutral atom qubits using the Rydberg blockade [10, 11]. Other gates may be designed, but the current technology already suffices for a "universal set."

To measure the individual qubits, laser pulses are used, like most operations in neutral atom quantum computing. To do this, the laser is simply tuned to a transition reachable by one state, say the |1> state, but not reachable by the other. Thus, if the atom fluoresces, it was measured in the |1> state. If it doesn't, then it was measured in the |0> state.

1.2 Dipole Trapping

To understand the physical process behind optical dipole trapping, we will follow the classical treatment of the interaction between far-detuned light and atoms as presented by Grimm, Weidemüller, and Ovchinnikov [13]. When a neutral atom is placed in an electric field, it will polarize as the forces from the field separate the negative electrons and the positive nucleus. Thus, the induced dipole moment of the atom is proportional to the applied electric field. If the applied field is that of an electromagnetic wave, we can write it in the standard form

$$\vec{E}(\vec{r},t)=\tilde{E}(\vec{r})e^{-i\omega t}\hat{e}, \tag{1}$$

where $\tilde{E}$ is the complex amplitude of the electric field, ω is the angular frequency, and ê is the unit vector in the polarization direction. In this case then, the induced dipole moment is

$$\vec{p}(\vec{r},t)=\tilde{p}(\vec{r})e^{-i\omega t}\hat{e}, \tag{2}$$

where the complex amplitude of the dipole moment, $\tilde{p}$, is related to $\tilde{E}$ by

$$\tilde{p}=\alpha\tilde{E}. \tag{3}$$

The constant α is the complex polarizability of the atom, and it depends on ω, the driving angular frequency of the electric field. The two components of the complex polarizability correspond to the two parts of the atom's interaction with the electric field: dispersion and absorption. The dispersive interaction gives rise to the optical dipole force that is used to trap the atom. It is described by the real part of α. The absorptive interaction causes scattering, which limits the quality of the traps. It is described by the imaginary part of α.

When an electric dipole is put in an electric field, the two will interact with the potential energy

$$U=-\vec{p}\cdot\vec{E}. \tag{4}$$

In this case, for an induced dipole in an oscillating electric field, we take the time average over many oscillations. We also insert a factor of one half to account for the dipole being induced rather than permanent. This gives

$$U=-\frac{1}{2}\langle\vec{p}\cdot\vec{E}\rangle, \tag{5}$$

which can be shown to simplify to

$$U=-\frac{1}{4}\mathrm{Re}(\alpha)|\tilde{E}|^2. \tag{6}$$

If we now use the definition of intensity,

$$I = \frac{1}{2} c \epsilon_0 |\tilde{E}|^2 , \tag{7}$$

where c is the speed of light and ϵ_0 is the vacuum permittivity, we can write

$$U = -\frac{1}{2 c \epsilon_0} \mathrm{Re}(\alpha) I . \tag{8}$$

This potential energy has an associated conservative force:

$$\vec{F}(\vec{r}) = -\nabla U(\vec{r}) = \frac{1}{2 c \epsilon_0} \mathrm{Re}(\alpha) \nabla I(r). \tag{9}$$

This is the force that will trap atoms in a well of the dipole potential energy. We have yet, however, to calculate α. To do so, we model the neutral atom as a simple harmonic oscillator, where the electron is elastically bound to the nucleus with a natural frequency ω_0. The oscillating electron will be damped by radiation according to Larmor's formula, which according to Griffiths [17] is

$$P = \frac{\mu_0 q^2 a^2}{6 \pi c} = \frac{q^2 a^2}{6 \pi \epsilon_0 c^3} , \tag{10}$$

where μ_0 is the vacuum permeability, q is the oscillating chage, and a is its acceleration. Also, to obtain the second form in Equation 10, we used the relationship

$$c = \frac{1}{\sqrt{\epsilon_0 \mu_0}} . \tag{11}$$

Thus, with our external oscillating electric field, we have the case of a driven, damped harmonic oscillator. The equation of motion is

$$\ddot{x} + \Gamma_\omega \dot{x} + \omega_0^2 x = -\frac{e}{m_e} \tilde{E} e^{-i \omega t} , \tag{12}$$

where e is the elementary charge, m_e is the electron mass, $\tilde{E}$ is once again the complex amplitude of the electric field, and ω is the frequency of the electric field's oscillation. The damping constant, Γ_ω, can be derived using the definition of power

$$P = -\frac{d \Xi}{dt} , \tag{13}$$

and assuming an exponential decay in the energy Ξ:

$$\Xi = \Xi_0 e^{-\Gamma_\omega t} . \tag{14}$$

Differentiating, we find

$$\frac{d \Xi}{dt} = \left(\Xi_0 e^{-\Gamma_\omega t} \right) (-\Gamma_\omega) = -\Gamma_\omega \Xi , \tag{15}$$

and thus by Equation 13,

$$P = \Gamma_\omega \Xi . \tag{16}$$

According to the simple harmonic oscillator model, the acceleration of the undamped electron is

$$a = -\omega^2 A \cos(\omega t) . \tag{17}$$

We can plug this into Larmor's formula, Equation 10, to find the power P. First we note that

$$a^2 = \omega^4 A^2 \cos^2(\omega t) . \tag{18}$$

Since we want a constant value, we must take the time average of this, and again use that the average of cosine squared is one half,

$$< a^2 > = \frac{1}{2}\omega^4 A^2. \tag{19}$$

Finally, we can use Equation 10 to find the power P:

$$P = \frac{e^2 \omega^4 A^2}{12\pi\epsilon_0 c^3}, \tag{20}$$

which by Equation 16 then gives

$$\frac{e^2 \omega^4 A^2}{12\pi\epsilon_0 c^3} = \Gamma_\omega \Xi. \tag{21}$$

Now, we can use the known expression for the energy of a simple harmonic oscillator,

$$\Xi = \frac{1}{2} m_e \omega^2 A^2, \tag{22}$$

to write

$$\frac{e^2 \omega^4 A^2}{12\pi\epsilon_0 c^3} = \Gamma_\omega \frac{1}{2} m_e \omega^2 A^2. \tag{23}$$

Finally, solving for Γ_ω we obtain the result

$$\Gamma_\omega = \frac{e^2 \omega^2}{6\pi\epsilon_0 m_e c^3}. \tag{24}$$

The differential equation, Equation 12, for a driven, damped harmonic oscillator has the known solution

$$x = \frac{-e}{m_e} \frac{1}{\omega_0^2 - \omega^2 - i\Gamma_\omega \omega} \tilde{E} e^{-i\omega t}, \tag{25}$$

Then, since $\tilde{p}$ points from the negative charge to the positive charge, we know that

$$\tilde{p} = -e x \ . \tag{26}$$

So then, using Equation 3, we finally obtain

$$\alpha = \frac{e^2}{m_e} \frac{1}{\omega_0^2 - \omega^2 - i\Gamma_\omega \omega}. \tag{27}$$

Now, if we put e^2/m_e in terms of Γ_ω, and introduce the on-resonance damping rate

$$\Gamma \equiv \left(\frac{\omega_0}{\omega}\right)^2 \Gamma_\omega, \tag{28}$$

we can write the polarizability as

$$\alpha = 6\pi\epsilon_0 c^3 \frac{\Gamma/\omega_0^2}{\omega_0^2 - \omega^2 - i(\omega^3/\omega_0^2)\Gamma}. \tag{29}$$

If we had instead taken the semi-classical approach to derive these equations, modeling the atom as a two-state quantum system in a classical electric field, we would have come to the same result except that Equations 24 and 28 would no longer have defined Γ, the spontaneous decay rate from the excited level. For many atoms however, including the alkali atoms commonly used for trapping, the classical formula is a good approximation to the real spontaneous decay rate.

Now that we have an expression for α, we can find the potential energy with Equation 8. First, take the

real part of α:

$$\Re(\alpha)=\frac{6\pi\varepsilon_0 c^3\Gamma}{\omega_0^2}\left(\frac{\omega_0^2-\omega^2}{(\omega_0^2-\omega^2)^2+(\omega^3/\omega_0^2)^2\Gamma^2}\right). \tag{30}$$

For the ω_0, ω, and Γ used in dipole trapping, it will usually be the case that

$$(\omega_0^2-\omega^2)^2 \gg (\omega^3/\omega_0^2)^2\Gamma^2. \tag{31}$$

So, we can make the approximation of dropping the second term in the denominator of $\Re(\alpha)$. Then, after simplifying the expression and plugging it into Equation 8, we finally obtain

$$U(\vec{r})=-\frac{3\pi c^2}{2\omega_0^3}\left(\frac{\Gamma}{\omega_0-\omega}+\frac{\Gamma}{\omega_0+\omega}\right)I(\vec{r}). \tag{32}$$

Note that this equation is resonant at both $\omega = \omega_0$, and at $\omega = -\omega_0$, due to the second term, the so-called "counter-rotating term." For most trapping experiments however, the laser light is tuned close enough to ω_0 that $\Delta << \omega_0$, where the detuning Δ is

$$\Delta \equiv \omega-\omega_0. \tag{33}$$

This makes the counter-rotating term negligible compared to the first term, and *U* simplifies to

$$U(\vec{r})=\frac{3\pi c^2}{2\omega_0^3}\frac{\Gamma}{\Delta}I(\vec{r}). \tag{34}$$

Equation 34 describes how carefully designed light patterns can create potential energy wells capable of trapping neutral atoms. First consider the "red-detuned" case where the laser's frequency is tuned below the resonant frequency of the atoms so $\Delta<0$. In this case, *U* will be minimized, that is most negative, when *I* is largest. Potential energy wells will occur for regions of high intensity surrounded on all sides by regions of low intensity. That is, red-detuned light allows for "bright spot" trapping.

Conversely, in the "blue-detuned" case, the laser's frequency is tuned above the atoms' resonant frequency, making $\Delta>0$. Then potential energy wells occur for regions of low intensity surrounded on all sides by regions of high intensity. In other words, blue-detuned light allows for "dark spot" trapping.

This classical derivation using a two-level atom is good for qualitative understanding, but insufficient for calculating the potential energy wells at the accuracy we need. For the actual analysis of the traps for qubit storage, we used a multi-level atom in a classical light field as presented by Gillen-Christandl and Copsey [18]:

$$U_{F,m_F}=-\frac{1}{4}\sum_q(-1)^q\left|E_{0q}\right|^2\times\sum_{F'}\alpha_{0,F',F}f_{F',F}\left(c^{F,1,F'}_{m_F,q,m_F+q}\right)^2. \tag{35}$$

Here, the *F* 's and m_F's refer to the hyperfine split substates of the electron, with a transition from *F* to *F′*. The q = +1,-1,0 and refers to the right circular, left circular, and linear polarization components of the electric field amplitude vector respectively. The $\alpha_{0,F',F}$ is the characteristic polarizability scalar, and in the SI units we used, it is given by

$$\alpha_{0,F',F}=-\frac{3\lambda^3}{32\pi^3}\frac{\Gamma}{\Delta_{F',F}}1.11\times10^{-10}\frac{\mathrm{Jm}^2}{\mathrm{V}^2}, \tag{36}$$

where $\Delta_{F',F}$ is the detuning from the *F* to *F′* transition. The $f_{F',F}$ is the relative oscillator strength of the *F* to *F′* transition, and is given by

$$f_{F',F} = (2J'+1)(2F+1)\left|\begin{Bmatrix} F' & I & J' \\ J & 1 & F \end{Bmatrix}\right|^2, \tag{37}$$

where the curly brace is the six-*J* symbol and *I* is the atom's nuclear spin quantum number. Finally, the *c* in the $U_{F,m}$ expression is the Clebsch-Gordon coefficient for the *F,m* to *F',m+q* dipole transition.

This gives the potential energy in Joules. In the atom trapping community, it is customary to express trapping potential energies in units of Kelvin, or millikelvin. To convert, we used

$$U_{F,m_F}(mK) = 1000\frac{2}{3k_B}U_{F,m_F}, \tag{38}$$

where $\frac{2}{3k_B}$ converts from Joules into Kelvin, and the factor of 1000 converts to millikelvin. We now have the necessary expressions to calculate the dipole potential energy for a given atom in a given intensity pattern. The pattern we investigated is composed of Gaussian beams, so a review of that topic is in order.

1.3 Gaussian Beams

The Gaussian beam solution to the wave equation is given by

$$\tilde{E}(\rho, z, t) = E_0\left(\frac{w_0}{w(z)}\right)e^{-\rho^2/w^2(z)}e^{ik\rho^2/2R(z)}e^{-i\tan^{-1}(z/z_0)}e^{i(kz-\omega t+\phi)}, \tag{39}$$

where $\tilde{E}$ is the complex electric field as a function of radial distance ρ, axial distance *z*, and time *t* [19]. The axial distance is measured from the beam waist w_0, where the beam is most narrow. The *k*, ω, and ϕ are the familiar wave number, angular frequency, and phase of the wave respectively. The amplitude of the wave is E_0. The Rayleigh range, z_0, coincides with how far the beam travels axially before it appreciably spreads radially. More will be said about it shortly. It is given by

$$z_0 = \frac{\pi w_0^2}{\lambda}, \tag{40}$$

where λ is the wave's wavelength. The spot size, *w*(*z*), is a measure of the beam's radius since it equals the radial distance at some *z* for which the intensity of the electromagnetic wave has dropped by a factor of $1/e^2$. It is given by

$$w^2(z) = w_0^2\left(1+\frac{z^2}{z_0^2}\right). \tag{41}$$

From Equation 41 we can see that the spot size at z_0 has spread to $\sqrt{2}w_0$. Lastly, the radius of curvature of the beam, *R*(*z*), is given by

$$R(z) = z\left(1+\frac{z_0^2}{z^2}\right). \tag{42}$$

From Equations 41 and 42, it is apparent that the spot size grows with increasing *z*, spreading the beam, and the radius of curvature initially shrinks with increasing *z*, producing more spherical wave fronts, and then begins to grow again, producing more planar wave fronts. The Rayleigh range, z_0, is the axial position where the radius of curvature is smallest. These behaviors have different rates along *z* depending on the beam's beam waist, w_0.

2 Geometric Properties of the Pattern

The intensity pattern we investigated results from two co-axial, counter-propagating Gaussian beams of the form of Equation 39, with different beam waists. The electric field of the beam with the smaller beam waist (taken to be the left-propagating beam in our investigation) drops off faster along the radial direction than the electric field of the beam with the larger beam waist. In this sense, the beam with the smaller beam waist is "inside" the other, and we shall refer to this arrangement as "nested Gaussian beams" for brevity. See Figure 1 for a diagram of this arrangement.

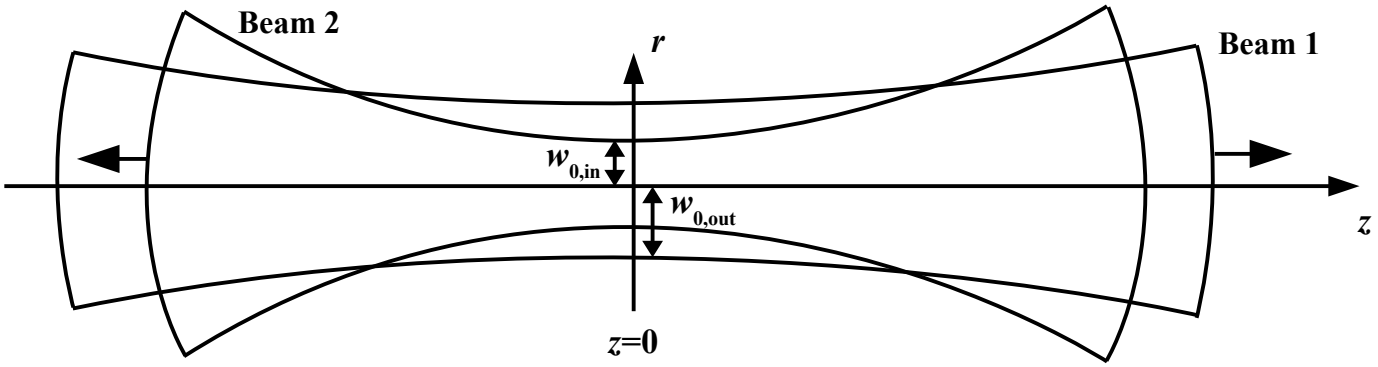

Figure 1: A schematic of nested Gaussian beams. The inner beam waist is $w_{0,\,in}$, while the outer beam waist is $w_{0,\,out}$. The inner beam is arbitrarily chosen to be the left-propagating beam. Note that the inner beam is only nested inside the outer beam for z sufficiently close to zero.

The resulting electric field from adding the two nested Gaussian beams is that of a standing wave with incomplete cancellation in the radial direction. That is, there are the expected nodes and anti-nodes along the propagation axis, but because the inner beam drops off more quickly in the radial direction, there is still light from the outer beam to either side of the nodes. Thus, the nodes of the standing wave pattern become a one-dimensional lattice of intensity wells of the configuration necessary for dark spot trapping. Figure 2a is an example of this intensity pattern for a beam waist pairing of 1 mm and 0.1mm. Note that all of the intensity graphs in this paper are actually plots of E^2, which by Equation 7 is proportional to intensity, hence the unusual units of $[\mathrm{V/m}]^2$ for intensity. Figure 2b shows how the nodes and anti-nodes are simple additions of two Gaussian profiles of different widths.

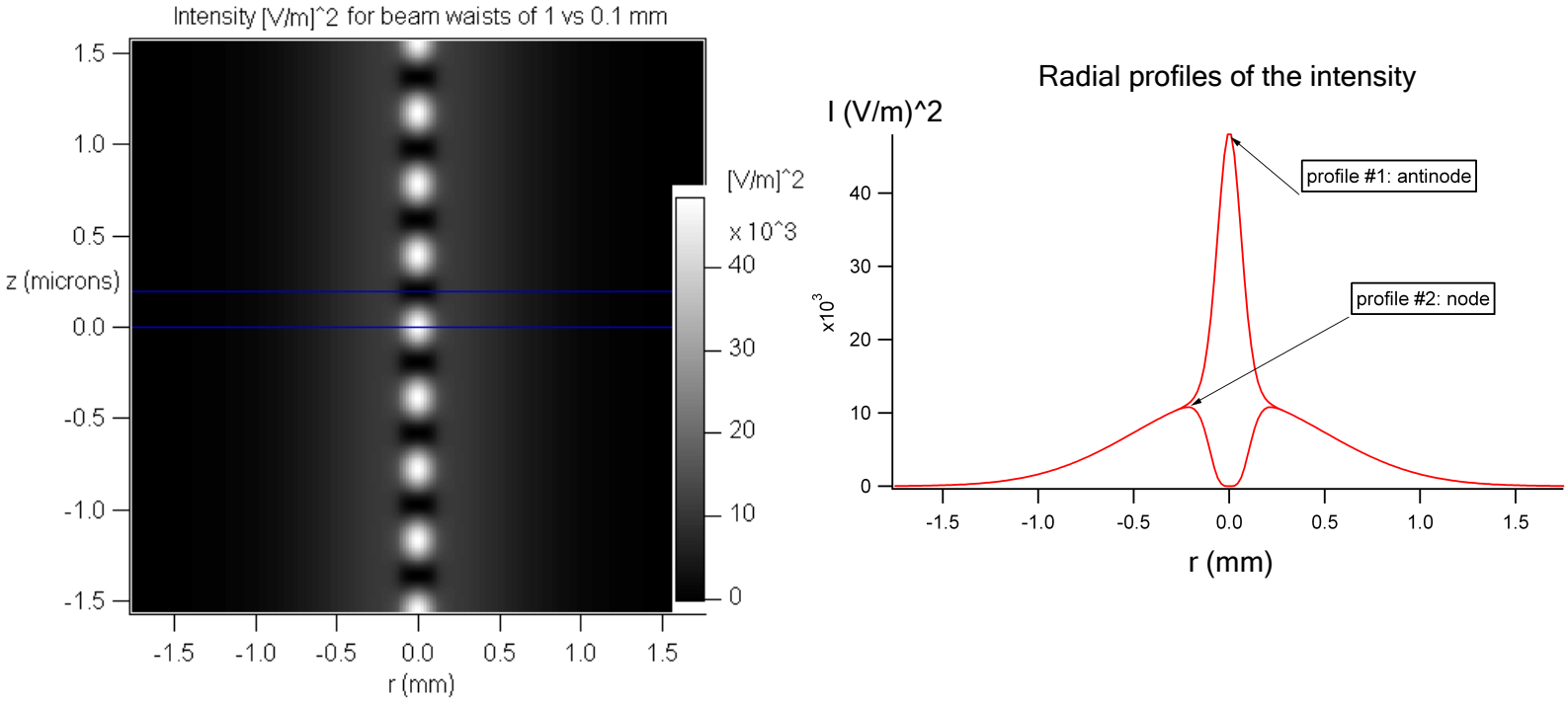

Figure 2: (a) E^2 (proportional to intensity) near z=0 for nested beams of beam waists 1mm and 0.1mm. The radial direction is horizontal and the axial direction is vertical. The blue lines mark where the profiles in 1(b) were taken. (b) Radial profiles of the intensity pattern through an anti-node and a node.

Recall from Section 1.3 that Gaussian beams with different beam waists diverge at different rates along z. This divergence coincides with a loss of the intensity wells for large z. In their analysis of this same nested beam pattern, Zemánek and Foot showed that the intensity wells disappear for $z > z_{max}$ [16]. They derive an analytical expression for z_{max} as the z-position where the radial edge of the intensity well goes to zero. This expression is

$$z_{max}^2 = k^2 \frac{w_{0,\text{out}}^{8/3} w_{0,\text{in}}^{8/3}}{w_{0,\text{out}}^{4/3} + w_{0,\text{in}}^{4/3}}, \tag{43}$$

where $k=2\pi/\lambda$ is the wavenumber of the beams, $w_{0,\text{out}}$ is the beam waist of the outer beam, and $w_{0,\text{in}}$ is the beam waist of the inner beam. They do not mention, however, the structure that appears in the intensity pattern as z approaches z_{max}. Figures 3-6 show four different z positions to portray the onset of what we deemed the "crescent structure", and how it leads to trap failure.

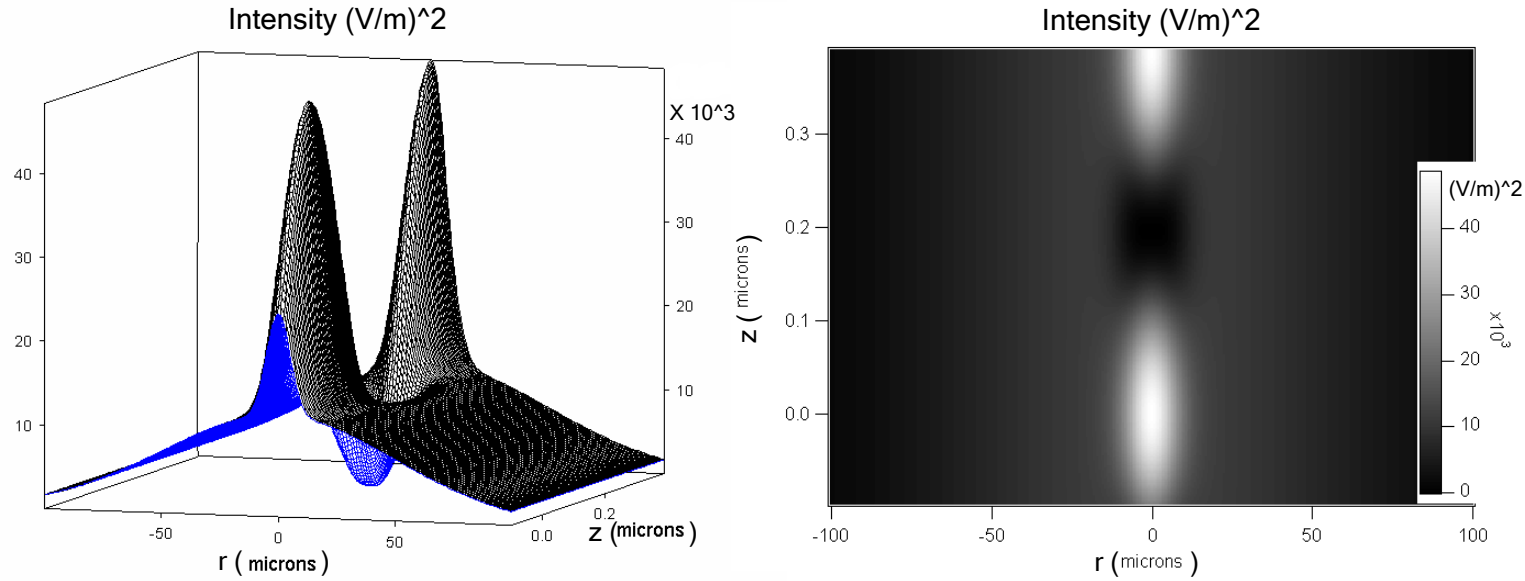

Figure 3: Surface plot (left) and image plot (right) of the intensity (E^2) pattern for nested Gaussian beams of beam waists 0.1mm and 0.01mm for a z-position of 0.

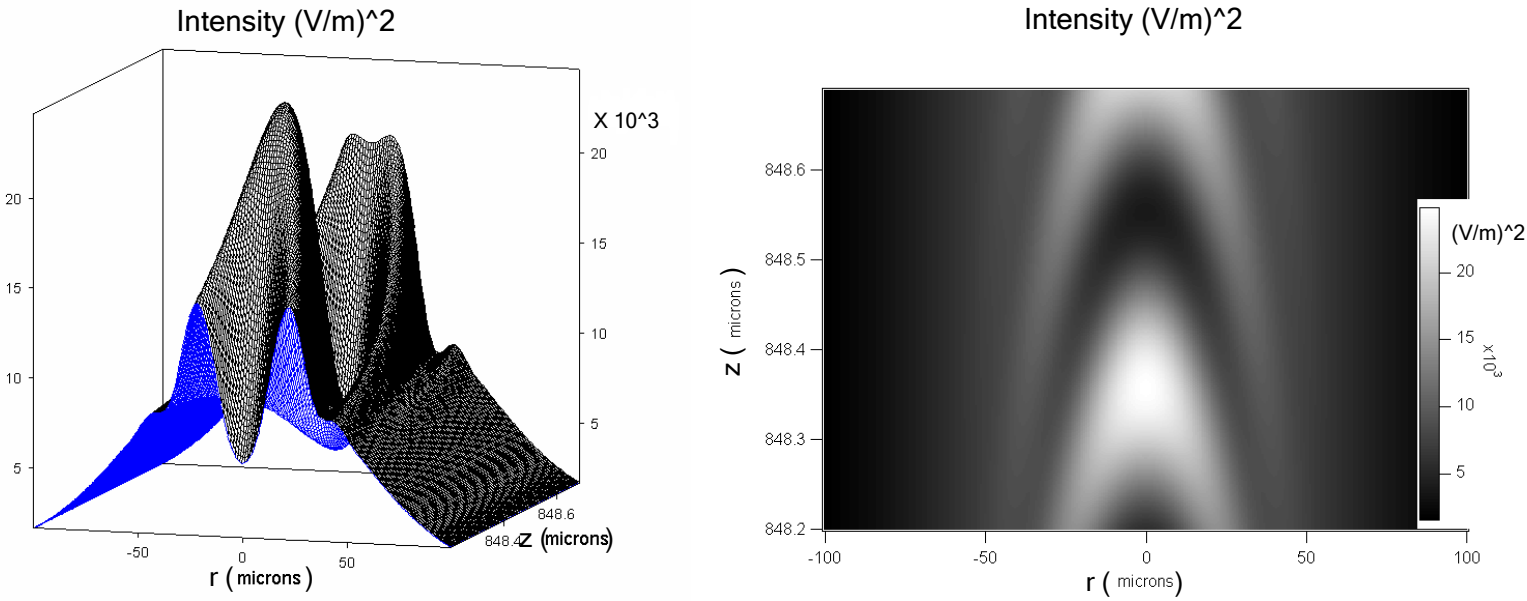

Figure 4: Surface plot (left) and image plot (right) of the intensity (E^2) pattern for nested Gaussian beams of beam waists 0.1mm and 0.01mm for a z-position of $z_{max}/20$.

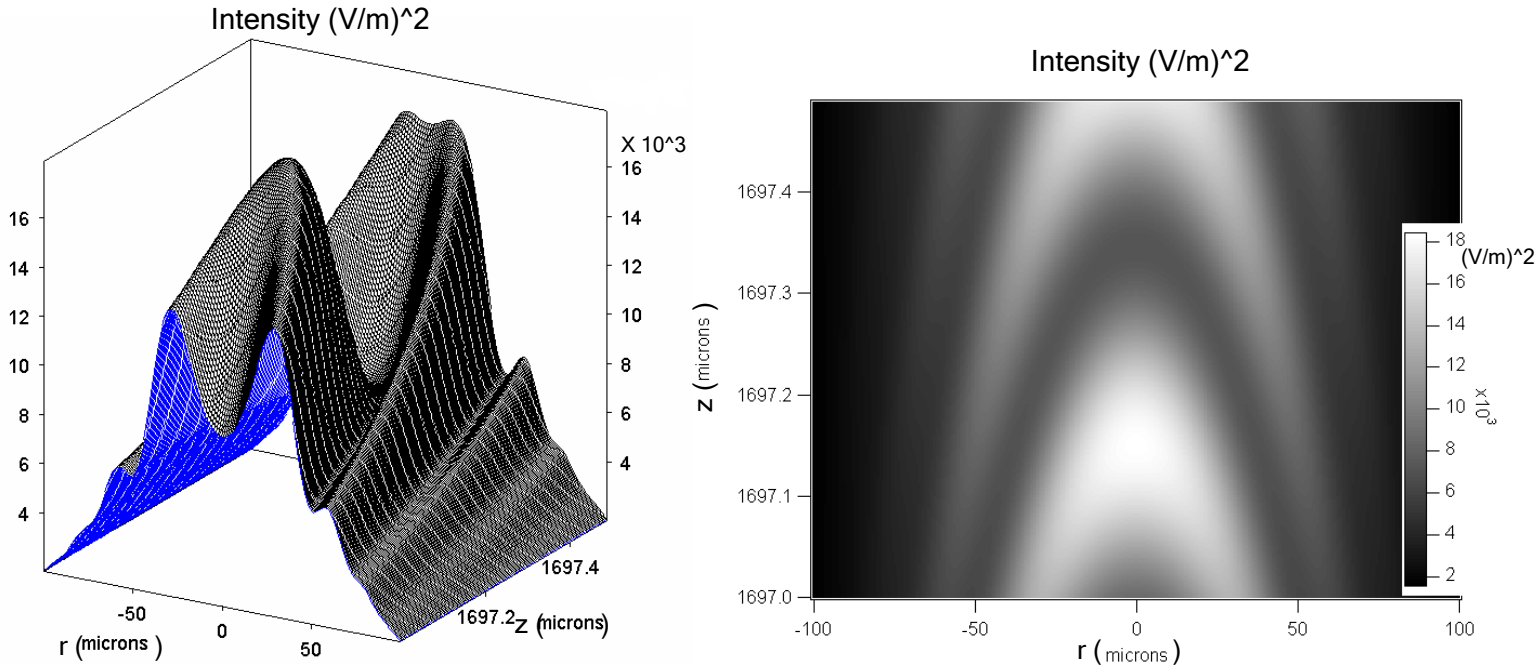

Figure 5: Surface plot (left) and image plot (right) of the intensity (E^2) pattern for nested Gaussian beams of beam waists 0.1mm and 0.01mm for a z-position of $z_{max}/10$.

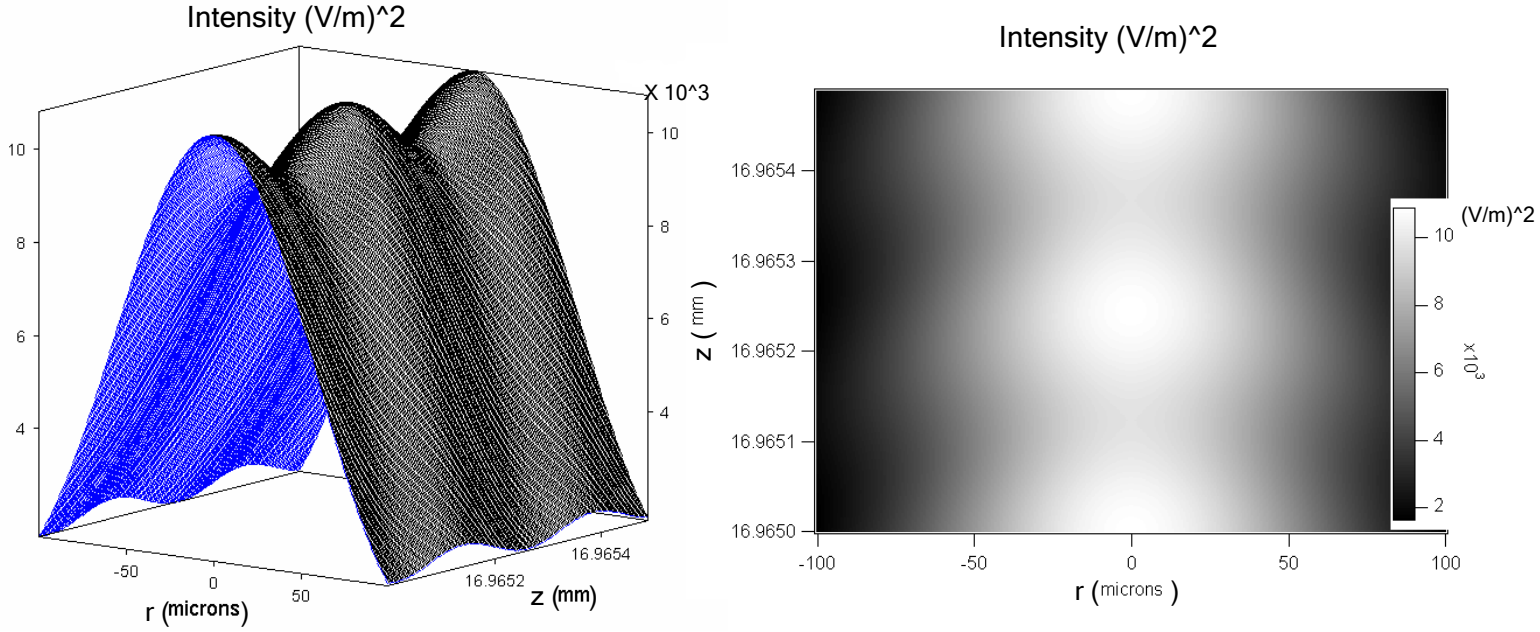

Figure 6: Surface plot (left) and image plot (right) of the intensity (E^2) pattern for nested Gaussian beams of beam waists 0.1mm and 0.01mm for a z-position of z_{max}.

As seen in Figure 3, the intensity near z=0 is the expected standing wave pattern with incomplete radial cancellation. However, by $z=z_{max}/20$ the crescent structure has begun to warp the intensity well and introduce low escape paths. The value of the intensity at the bottom of the well has also begun to rise, as predicted by Zemánek and Foot [16]. This rising of the minimum greatly limits the effectiveness of the traps for large z values, and should make the wells infeasible for quantum computation before z_{max} is reached. At $z=z_{max}/10$, the well is still present, but it is only slightly lower than the escape paths. Finally, at z_{max} there is no intensity well whatsoever, and the axial intensity minima are not much lower than the axial intensity maxima.

Another important geometric property of the pattern is the dependence of trap depth and width on the beam waist ratio. As might be anticipated, and as shown in Figure 7, the trap depth increases for smaller ratios of inner beam waist to outer beam waist. This is because, compared to the outer beam, the inner beam drops off faster radially for smaller beam waist ratios. This leaves more light for radial confinement in the incomplete cancellation. Zemánek and Foot also found that, for smaller beam waist ratios, the traps broaden more as z moves away from 0 [16]. This makes sense as beams with more disparate beam waists have more disparate divergence rates.

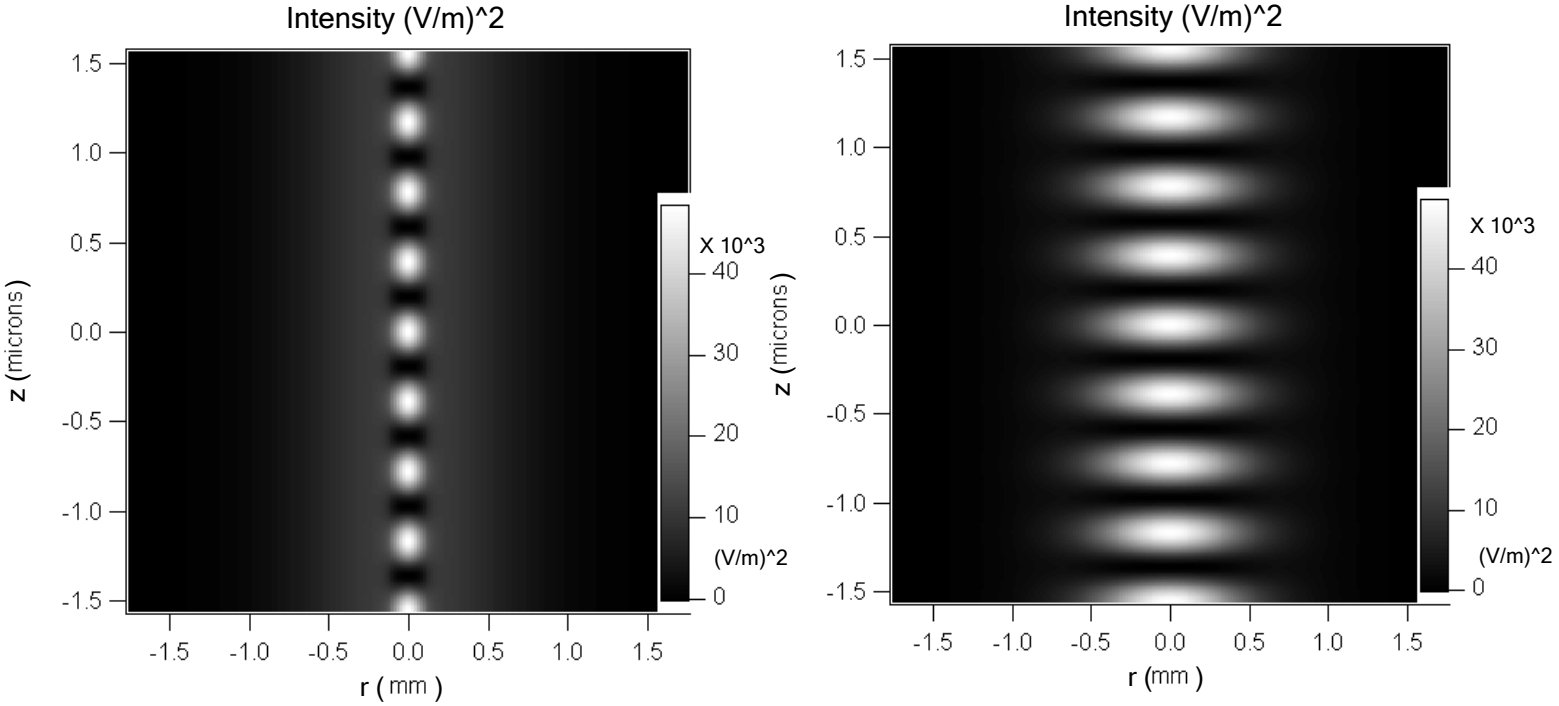

Figure 7: Intensity (E^2) patterns for nested Gaussian beams of beam waists 1mm and 0.1mm (left) and for beam waists of 1mm and 0.5mm (right).

Lastly, it is important to note that the beam waists used in the examples so far all produce wells that are much larger in the radial direction than in the axial direction. This is because, in the axial direction, the traps follow the standing wave periodicity of two traps per wavelength. So, for the 780 nm light used to trap rubidium, there is a distance of 0.39 microns between traps. However, in the radial direction, the trap width is determined by the beam waists involved. This is on the order of tenths of microns in the examples so far. Indeed, the radial dimension will be much larger than the axial dimension unless the beams are focused to beam waists on the order of a wavelength. Figure 8 shows the intensity for

nested beams with beam waists of 2 microns and 0.5 microns with the same scaling in the radial and axial directions. Even if the beams' diameters were focused to the diffraction limit of approximately one wavelength, the radial dimension would still be twice the size of the axial dimension as the traps occur every λ/2. Note this would also greatly reduce the value of z_{max}. If an extremely large number of traps is desired, then that will limit how far the beams can be focused.

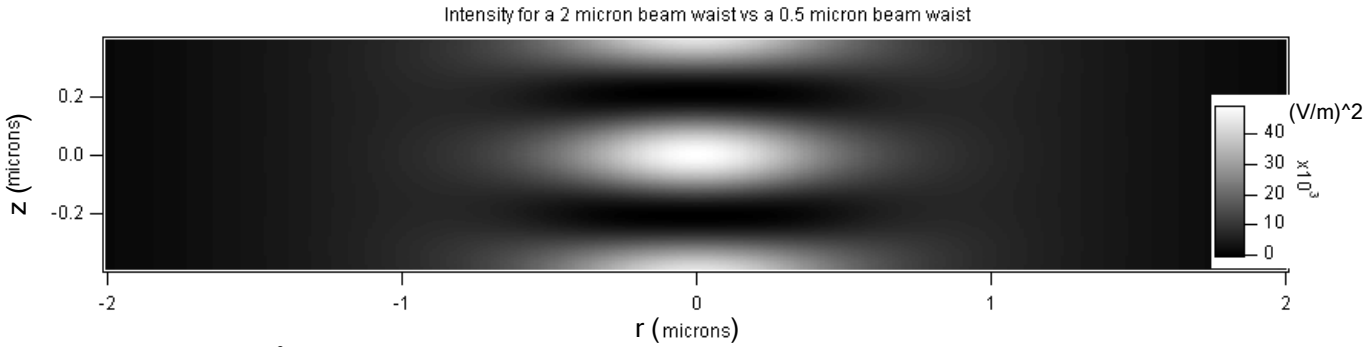

Figure 8: Intensity (E^2) pattern for nested Gaussian beams of beam waists 2 microns and 0.5 microns with even scaling horizontally and vertically.

These are the general geometric properties of the nested Gaussian beam light pattern. The next section discusses the methods used to computationally investigate this pattern.

3 Computational Methods

3.1 Calculating the Electric Field

For our computational investigation of the nested Gaussian standing wave pattern, we used *Mathematica* for calculations, and Igor for image production. In our *Mathematica* codes, we added two counter-propagating beams by adding Equation 39 for a right-propagating beam to the same equation with the substitution z→-z for a left-propagating beam. Each beam's properties were individually adjustable, and we set all of the parameters the same except for the beam waists for the basic nested standing wave pattern.

Our codes were built around the specific case of trapping ^{87}Rb, an alkali metal commonly used for neutral atom trapping and the production of qubits. Its atomic properties and electronic state structure were built into the code. The energy of the trapping transition of ^{87}Rb corresponds to photons of wavelength 780nm, so this was the wavelength of light used in the code.

Setting t=0 to view only the maximum of the oscillating field, our electric field became a function of ρ and z. So to produce 2D cross-sections of the electric field strength, we stepped through a symmetric ρ interval about ρ=0 and a specified z interval, calculating $\tilde{E}$ at each point. The resulting complex matrix for $\tilde{E}$ was then used to calculate matrices for the intensity and dipole potential energy. Because of the inherent radial symmetry of this light arrangement, such 2D cross-sections are sufficient to fully describe the pattern in general.

3.2 Polarization of the Electric Field

I have not yet commented on the polarizations we set for our counter-propagating beams. This is because they require some explanation. All of the vector information for the electric field is contained in the amplitude E_0, or more accurately $\vec{E}_0$. We set the beams to have aligned linear polarizations of 45° by setting

$$\vec{E}_0 = \frac{E_0}{\sqrt{2}}\hat{x} + \frac{E_0}{\sqrt{2}}\hat{y} \tag{44}$$

for each beam. That is, the right-propagating beam had a polarization of 45°, but the left-propagating beam had a polarization of -45° from its perspective, so that the two vectors would overlap and create the standing wave pattern. In the code, however, everything was calculated from the right-propagating beam's perspective, so the x- and y-components of both beams were the same, with the left-propagation being enforced by setting z→-z for that beam.

Further complicating matters is that, while defining $\vec{E}_0$ sets the polarization at the beam waist, it does not hold for *z* values other than zero. Recall that the Poynting vector $\vec{S}$ for electromagnetic radiation points in the direction of energy flow, with a magnitude equal to the intensity of the light. As the Gaussian beam diverges, the Poynting vector in off-axis positions diverges from the horizontal. The Poynting vector is always perpendicular to the electric field, so as it diverges, the polarization of the electric field diverges from $\vec{E}_0$.

To simplify our calculations, we made the approximation that the electric field polarization vector maintains no z-component for all values of *z*. That is, it had no component parallel to the axis of propagation. So, we calculated two complex matrices for the electric field, one for the x-component and another for the y-component.

To justify the validity of this approximation, consider Equation 41 for spot size. After taking the square root, the positive branch is

$$w(z) = w_0\sqrt{1+\frac{z^2}{z_0^2}}. \tag{45}$$

The negative branch follows the same behavior reflected about the z-axis. The derivative of this function is

$$\frac{dw}{dz} = \frac{w_0}{z_0}\frac{z}{\sqrt{z_0^2+z^2}}. \tag{46}$$

So we can see as $z \to \infty$, $\frac{dw}{dz} \to \frac{w_0}{z_0}$. Since the derivative gives the slope of the tangent at any z, this function gives a slope that forms the same angle with the z-axis as the angle between the Poynting vector at $\rho = w(z)$ and the propagation axis. See Figure 9. This angle is then

$$\theta(z) = \arctan\left(\frac{dw}{dz}\right). \tag{47}$$

By the geometry of transverse waves, this is also the angle between the electric field polarization vector and the vertical x-axis (picking the convenient coordinate system, as in Figure 9, where $\vec{E}$ lies in the xz-plane).

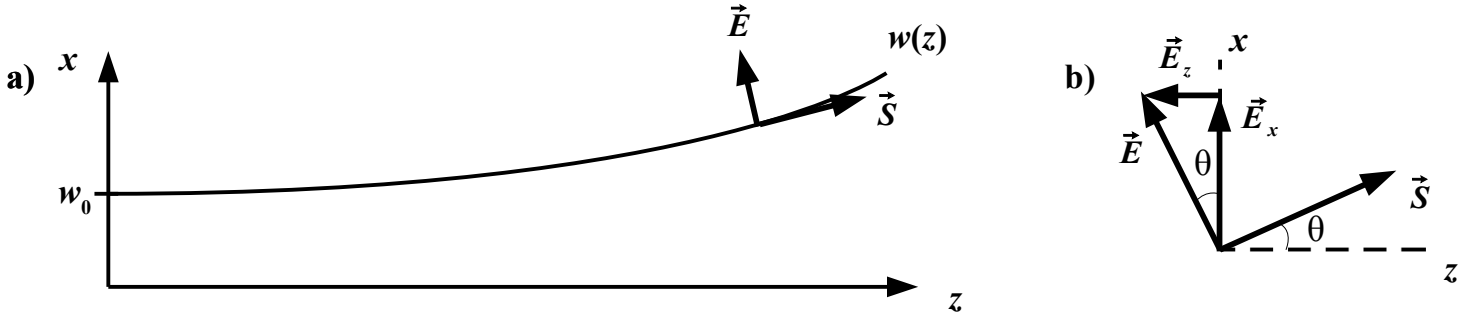

Figure 9: (a) A schematic of the spot size function $w(z)$ for positive z and x. At a given z-position, the tangent to $w(z)$ will point in the same direction as the Poynting vector $\vec{S}$. (b) A larger image of the angle $\vec{S}$ forms with the horizontal, and $\vec{E}$ forms with the vertical for nonzero values of z.

So for this positive branch (x>0) the z-component of $\vec{E}$ is

$$E_z = -E\sin(\theta). \tag{48}$$

Finally then, the largest value of E_z will occur in the limit as $z \to \infty$, which is

$$E_z = -E\sin\left(\arctan\left(\frac{w_0}{z_0}\right)\right). \tag{49}$$

So for beam waists of 1 mm and 0.1 mm respectively we get

$$\begin{aligned}\frac{E_z}{E} &= -\sin\left(\arctan\left(\frac{10^{-3}}{4.03}\right)\right) = -0.00025 \\ \frac{E_z}{E} &= -\sin\left(\arctan\left(\frac{10^{-4}}{0.0403}\right)\right) = -0.0025\end{aligned} \tag{50}$$

Thus, it is reasonable to neglect the z-component of the electric field.

3.3 Calculating the Dipole Potential Energy

After the electric field matrices were calculated, the next step was to calculate the dipole potential energy of ^{87}Rb atoms placed in such a field. As explained in Section 1.2 we used Equations 35-38 to calculate this potential energy.

First, we had to convert the electric field from the Cartesian coordinates it was calculated in to the spherical coordinates (circular polarization components) Equation 35 requires. The relation between the Cartesian and spherical components is [18]

$$\begin{aligned}E_{0-1} &= \frac{1}{\sqrt{2}}(E_{0x} + iE_{0y}), \\ E_{00} &= E_{0z}, \\ E_{0+1} &= \frac{1}{\sqrt{2}}(-E_{0x} + iE_{0y}).\end{aligned} \tag{51}$$

Once this conversion was applied to our electric field matrices, we used the Equations 35-38 to calculate the matrix of potential energy values over the selected ρ and z ranges. Because the potential energy depends on the specific F,m_F state of the valence electron, we actually computed several

potential energy matrices, one for each hyperfine split ground state. These were $(F,m_F) = (1,-1), (1,0), (1,1), (2,-2), (2,-1), (2,0), (2,1), (2,2)$. For consistency, we chose to analyze the (1,-1) case in each of the different z-position and beam waist configurations we investigated.

3.4 Analyzing the Potential Energy Wells

To analyze the properties of the potential energy wells, we modeled them as simple harmonic oscillator potential energies. The potential energy of a simple harmonic oscillator moving in the x-direction is

$$U = \frac{1}{2} m \omega^2 x^2, \tag{52}$$

where for us, m is the mass of a rubidium atom, and ω is $2\pi f_0$, where f_0 is the trap frequency. Drawing an analogy to a mass-spring system, f_0 would be the frequency with which the mass oscillates about its equilibrium position.

To model our traps as harmonic oscillator potential energies, we calculated a 1D line of data through a given trap, and fit a quadratic function to the data points using a second *Mathematica* code. From the coefficients of this fit, we then calculated the trap frequency and other properties which characterized the trap. Because of the symmetries of the intensity pattern near z=0, it was sufficient to analyze one line of data through the trap's minimum in the radial direction, and one in the axial direction. These two analyses then describe the strong confinement in the axial dimension, and the most likely escape path in the more weakly confined radial direction. Recalling the discussion in Section 2, it is clear that this simple choice of data lines will not fully characterize traps far from z=0, but for this paper we restrict our analysis to values of z that are sufficiently small. As we shall see, "sufficiently small" can be an appreciable range.

The potential energy wells are not perfectly harmonic, so while the bottom of the well may be best described by one quadratic function, the sides are best described by another. So, we actually performed several fits to the data, each one including a different number of data points around the minimum. The further from the minimum, the higher up the walls of the trap the data points were, and the higher the energy difference between the top and bottom of our investigated range. In this way, we obtained trap properties for different possible energy ranges of the trapped atoms. Figure 10 shows a sample of the fits over the different data ranges for beam waists of 1mm and 0.1mm at z=10mm along the radial direction.

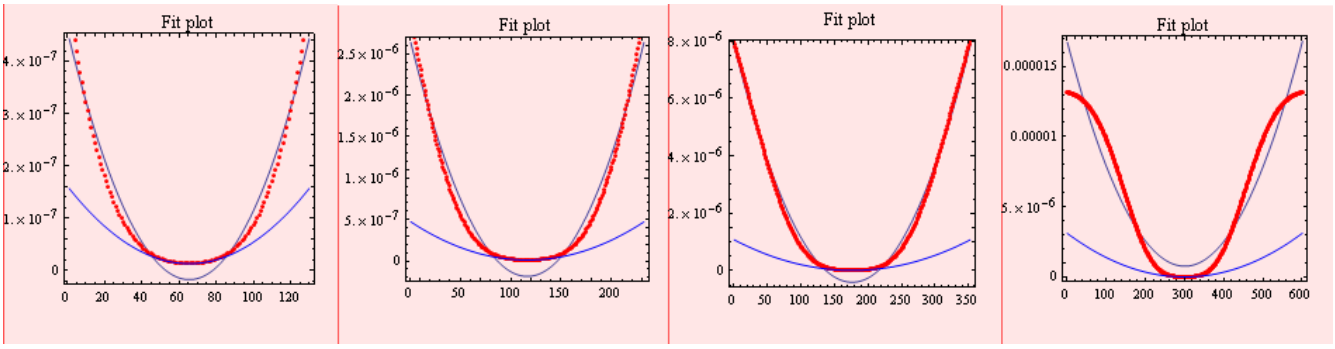

Figure 10: A sampling of the fits over different data ranges for nested beams of beam waists 1mm and 0.1mm at z=10mm along the radial direction. The vertical axis is the potential energy in millikelvin. The horizontal axis shows the number of data points included out of the entire calculated line.

As mentioned above, the first trap property we calculated was the trap frequency f_0. The energy levels of a quantum harmonic oscillator are evenly spaced, and given by

$$E_n = \left(n + \frac{1}{2}\right)\hbar\omega = \left(n + \frac{1}{2}\right)h f_0. \tag{53}$$

So from the trap frequency, we calculated the energy difference between oscillator levels

$$\Delta U_{osc} = \frac{h f_0}{k_B}, \tag{54}$$

where the factor of k_B converts from Joules to Kelvin, as before. For quantum computation, as discussed in Section 1.1, the atom acting as a qubit must stay in the same state for a very long time (long decoherence time). So it is very important that the oscillator energy level difference be large enough, and the trapped atoms cold enough, that a transition between oscillator levels is very infrequent.

The next trap property calculated was the ground state size, β_{osc}. The ground state size is the $1/e$ half width of the probability density for the wavefunction in the motional harmonic oscillator ground state. This length is calculated by

$$\beta_{osc} = \sqrt{\frac{\hbar}{2\pi f_0 m}}, \tag{55}$$

where m is the mass of a ^{87}Rb atom.

Lastly, we also calculated the difference between the potential energy at the upper edge of the trap along the line we chose, and the minimum of the well. This ΔU_{trap} gives a measure of how cold atoms have to be to be confined in the well at all. Since the radial confinement is weaker, this value in the radial direction sets the limit on how cold atoms have to be in order to be trapped.

4 Results

We investigated three different cases in detail to get a sense of the trap properties for different beam waists and z-positions. The first trap in the positive z-direction (z=0 is an anti-node) for beam waists of 1mm and 0.1mm was taken as the base case. This was compared to the trap at z just under 10mm for those same beam waists, and the first trap in the positive z-direction for beam waists of 0.1mm and 0.01mm. As discussed before, the methods we employed were not suitable for the crescent regime. Figure 11 shows that the crescent structure had not significantly altered the traps at 10mm for 1mm and 0.1mm beam waists, so our analysis was still valid. Note also that in the range -10mm< z <10mm there are approximately 51,000 traps, and that $z_{max} \approx 300\text{mm}$ for this arrangement. So even though z must be kept sufficiently small to avoid the crescent structure, a large number of traps may still be obtained by using sufficiently large beam waists.

Table 1 presents the trap properties in the radial and axial directions for the three cases listed above. All of these cases used an incident intensity of 1.6 mW/cm^2 which gives E_0=110 V/m, and a detuning of Δ=1000Γ, where Γ=2π×6 MHz, the linewidth of the trapping D2 transition in rubidium

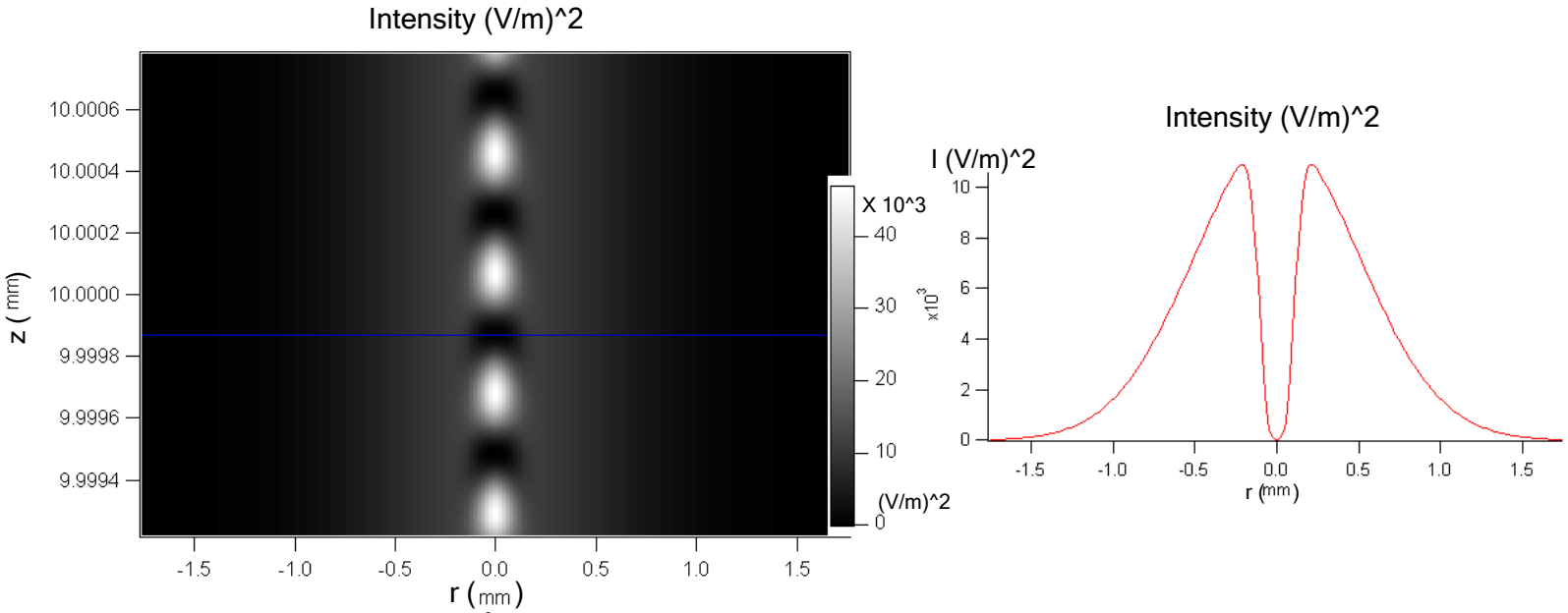

Figure 11: The intensity (E^2) pattern and profile through the analyzed trap for nested beams of beam waists 1mm and 0.1mm at z=10mm. Note that the crescent structure has begun to appear, but has not invalidated the radial trap analysis.

Beam waists	Direction	f_0 [Hz]	ΔU_{osc} [nK]	β_{osc} [μm]
1 vs 0.1 mm z = 0 trap	axial	5200, 5000, 4300	250, 240, 210	0.15, 0.15, 0.17
	radial	1.2, 2.0, 1.9	0.06, 0.10, 0.09	9.7, 7.6, 7.7
1 vs 0.1 mm z = 10mm trap	axial	5100, 4900, 4100	250, 230, 200	0.15, 0.15, 0.17
	radial	1.3, 2.0, 2.0	0.07, 0.10, 0.10	9.3, 7.6, 7.7
0.1 vs 0.01mm z = 0 trap	axial	5200, 5000, 4300	250, 240, 205	0.15, 0.15, 0.17
	radial	12, 20, 19	0.59, 0.96, 0.93	3.1, 2.4, 2.4

Table 1: The trap properties for nested beams of beam waists 1mm and 0.1mm at z just greater than 0 and just less than 10mm, and for beam waists of 0.1mm and 0.01mm at z just greater than 0. The three entries in every cell are the values for data ranges that span up to the bottom of the well, the middle of the well, and the top of the well in that order. In each case, ΔU_{trap} = 12 nK.

In Table 1 we can see the behavior of the traps for different beam waists and z-positions. First of all, there was only a change of a few percent in the trap properties when z was increased to 10mm from the base case. This indicated that keeping z below the crescent regime also maintained the maximal quality achieved at the beam waist. As discussed earlier, however, this z-range decreases with smaller beam waists and smaller inner to outer beam waist ratios as the traps widen with z.

Next, notice that the trap properties in the axial directions did not noticeably change when the beam waists were decreased (maintaining the same ratio). This would be expected since the traps followed the standing wave pattern in the axial direction near z=0, and focusing the beams only tightens the radial dimension.

The trap properties in the radial dimension changed significantly with beam waist. For the same beam waist ratio, but with each individual beam waist reduced by a factor of 10, the trap frequency and the spacing between vibrational levels both increased by a factor of 10. The ground-state size decreased by a factor of $\sqrt{10}$. That is, there was a direct relationship between beam waist scale and trap quality. This predicts higher quality traps are achievable by focusing the beam waists to the wavelength scale.

In every case, ΔU_{osc} for the radial dimension was extremely small. Even a typical Bose-Einstein condensate (BEC) temperature of 50 nK would be much too large to keep the atom confined to one vibrational energy level. This would cause problems for quantum computation, but ΔU_{osc} should increase for tighter radial confinement, i.e. smaller inner to outer beam waist ratios, and smaller beam waists. More investigation into this is needed. For the axial dimension, however, ΔU_{osc} was suitable for trapping atoms of typical BEC temperatures in the vibrational ground state with a low probability of vibrational level transition.

Finally, consider the trap depth ΔU_{trap} which is the potential energy difference between the bottom of the well and the top of the most weakly confined "escape" path. For all three configurations shown in Table 1, ΔU_{trap} is limited by the radial confinement to 12 nK. This is too low to trap even typical BEC atoms in the potential energy wells. However, this was likely due to the choice of beam intensity. We used 1.6 mW/cm^2 as the intensity of the two nested beams, but intensities five orders of magnitude larger than this are reasonable for highly focused diode laser beams. Recalling Equation 34, the trap depth is proportional to intensity. Thus an increase in intensity by a factor of 10^5 would bring the trap depth up to the order of one millikelvin, a much more reasonable value for atom trapping. More investigation is needed to explore this.

Conclusion

We computationally investigated the intensity pattern produced by two counter-propagating Gaussian beams of differing beam waists. This pattern was analyzed for feasibility as a 1D lattice of blue-detuned dipole traps for neutral atom quantum computing.

For z-positions far from z=0, it was found that the differing divergence rates with z of the two beams led to a crescent shaped structure of the traps. This structure introduced low escape paths for trapped atoms, and gradually worsened as z increased, eventually destroying the traps altogether. For suitably small z-positions, the traps maintained their quality from z=0.

Unless the beams were focused to beam waists on the order of a wavelength, the radial dimension of the traps was much larger than the axial dimension. This led to much worse trap properties in the radial dimension in the cases investigated. While the traps were capable of confining BEC atoms for quantum computation in the axial dimension, the traps were incapable of confining BEC or more energetic atoms and were poor for quantum computation in the radial dimension. A smaller inner to outer beam waist ratio led to deeper traps, and smaller beam waists led to better radial trap properties, but both of these also reduced the quality of traps for large z-positions.

For the individual beam intensity chosen, the traps were too weak to confine atoms in the radial dimension. The properties of the traps should improve, however, for increased intensities. Our next step is to analyze the traps at higher intensities, and find a beam waist pair that maximizes trap quality

without too greatly reducing the *z* trapping range.

We also plan to make calculations of the scattering rate for these traps, one of the main sources of decoherence for atoms in dipole traps. The trap properties in the crescent region also need to be determined to find exactly when they cease to be feasible for storing qubits. Lastly, we plan to investigate nested Gaussian beams of slightly different wavelengths, for which the nodes move along *z* with time, creating an atomic conveyor belt.

References

[1] I. H. Deutsch, G. K. Brennen, and P. S. Jessen. "Quantum Computing with Neutral Atoms in an Optical Lattice." Fortschr. Phys. **48** 9-11, 925-943 (2000).

[2] J. F. Poyatos, J. I. Cirac, and P. Zoller. "Schemes of Quantum Computations with Trapped Ions." Fortschr. Phys. **48** 9-11, 785-799 (2000).

[3] P. Grangier, G. Reymond, and N. Schlosser. "Implementations of Quantum Computing Using Cavity Quantum Electrodynamics Schemes." Fortschr. Phys. **48** 9-11, 859-874 (2000).

[4] D. G. Cory, et. al. "NMR Based Quantum Information Processing: Achievements and Prospects." Fortschr. Phys. **48** 9-11, 875-907 (2000).

[5] B. E. Kane. "Silicon-based Quantum Computation." Fortschr. Phys. **48** 9-11, 1023-1041 (2000).

[6] Y. Makhlin, G. Schön, A. Shnirman. "Josephson-Junction Qubits." Fortschr. Phys. **48** 9-11, 1043 1054 (2000).

[7] A. Barenco. "Quantum Physics and Computers." Contemporary Physics **37** No. 5 375-389 (1996).

[8] P. W. Shor. "Polynomial-Time Algorithms for Prime Factorization and Discrete Logarithms on a Quantum Computer." Siam J. Comput. **26** No. 5, 1484-1509 (1997).

[9] L. K. Grover. "Quantum mechanics helps in searching for a needle in a haystack." Phys. Rev. Lett. **79** No. 2, 325-328 (1997).

[10] P. Grangier, and A. Browaeys, et. al. "Entanglement of Two Neutral Atoms Using Rydberg Blockade." Phys. Rev. Lett. **104**, 010502 (2010).

[11] L. Isenhower, E. Urban, X. L. Zhange, A. T. Gill, T. Henage, T. A. Johnson, T. G. Walker, and M. Saffman. "Demonstration of a Neutral Atom Controlled-NOT Quantum Gate." Phys. Rev. Lett. **104**, 010503 (2010).

[12] D. P. DiVincenzo. "The Physical Implementation of Quantum Computation." Fortschr. Phys. **48**, 9-11, 771-783 (2000).

[13] R. Grimm, M. Weidemüller, and Y. B. Ovchinnikov. "Optical Dipole Traps for Neutral Atoms." Adv. At. Mol. Opt. Phys. **42**, 95-170 (2000).

[14] Y Miroshnychenko, W Alt, I Dotsenko, L Förster, M Khudaverdyan, A Rauschenbeutel and D Meschede. "Precision preparation of strings of trapped neutral atoms." New J. Phys. **8**, 191 (2006).

[15] N. Davidson, H. J. Lee, C. S. Adams, M. Kasevich, and S. Chu. "Long Atomic Coherence Times in an Optical Dipole Trap." Phys. Rev. Lett. **74** No. 8, 1311-1314 (1995).

[16] P. Zemánek and C.J. Foot. "Atomic dipole trap formed by blue detuned strong Gaussian standing wave." Optics Comms. 146, 119-123 (1998).

[17] D. J. Griffiths. *Introduction to Electrodynamics*, 3d ed. Upper Saddle River: Prentice Hall, 2005. Ch 11.

[18] K. Gillen-Christandl and B. D. Copsey, "Polarization-dependent atomic dipole traps behind a circular aperture for neutral-atom quantum computing." Phys. Rev A **83**, 023408 (2011).

[19] F. L. Pedrotti, L. M. Pedrotti, and L. S. Pedrotti. *Introduction to Optics*, 3d ed. San Franscisco: Pearson Addison Wesley, 2007. Ch 27.